IEEE Photonics Journal
An IEEE Photonics Society Publication

Open Access

Large-Dynamic-Range Dual-Parameter Sensor Using Broad FSR Multimode Photonic Crystal Nanobeam Cavity

Volume 10, Number 5, September 2018

Chao Wang
Zhongyuan Fu
Fujun Sun
Jian Zhou
Huiping Tian

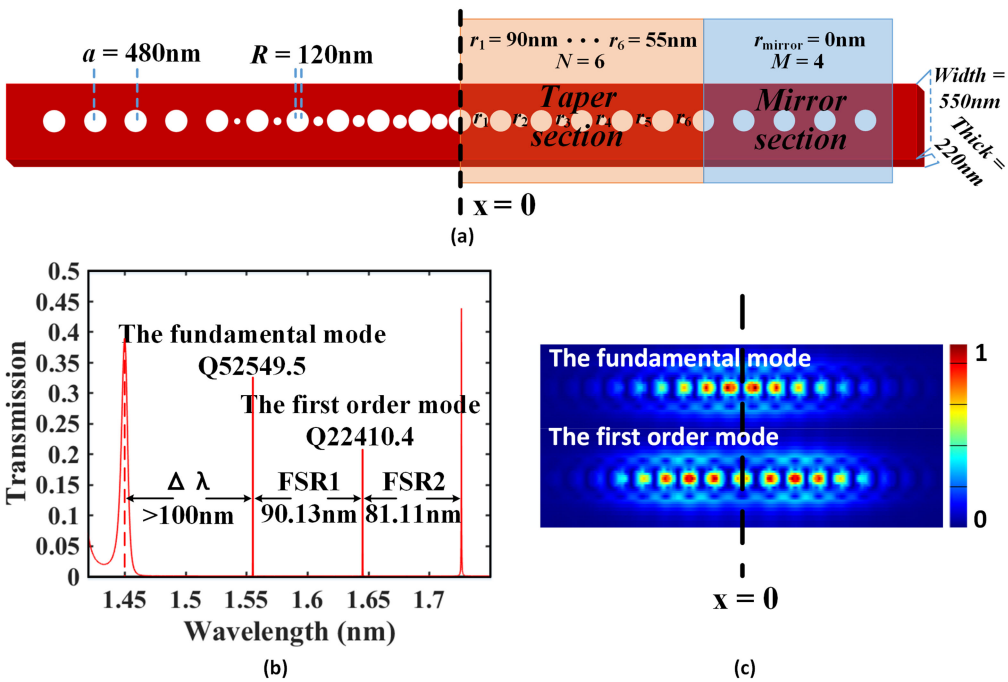

DOI: 10.1109/JPHOT.2018.2865510
1943-0655 © 2018 IEEE

Large-Dynamic-Range Dual-Parameter Sensor Using Broad FSR Multimode Photonic Crystal Nanobeam Cavity

Chao Wang, Zhongyuan Fu, Fujun Sun, Jian Zhou, and Huiping Tian

State Key Laboratory of Information Photonics and Optical Communications, Beijing Key Laboratory of Space-Ground Interconnection and Convergence, School of Information and Communication Engineering, Beijing University of Posts and Telecommunications, Beijing 100876, China

DOI:10.1109/JPHOT.2018.2865510

Manuscript received July 6, 2018; revised August 8, 2018; accepted August 10, 2018. Date of publication September 13, 2018; date of current version October 1, 2018. This work was supported by NSFC (No. 61372038 and No. 61431003), and Joint Laboratory for Undersea Optical network, Beijing University of Posts and Telecommunications, Beijing, China. Corresponding author: Huiping Tian (e-mail: hptian@bupt.edu.cn).

Abstract: We theoretically propose an ultracompact large-dynamic-range dual-parameter sensor using a broad free spectral range (FSR) multimode photonic crystal nanobeam cavity (MM-PCNC). In the multimode regime, each resonant mode is exploited as an independent sensing channel. Broad FSR (>100 nm) is achieved by PCNC consisting of composite lattice cells (CLCs). The CLC is designed for the special bands property enabling the excitation of multiple resonant modes with broad FSR possible. Notably, an interesting stability of the mirror strength is achieved for the CLC, which provides a new perspective for further optimizing ultracompact PCNCs with high quality factor (Q) and broad FSR. Additionally, due to the special structure of the CLC, the energy of resonant modes can be effectively localized in the low dielectric area, which are quantitatively indicated by the calculated optical overlap integrals, resulting in strong light-matter interactions. Simultaneous detection of the refractive index (RI) and temperature is conducted by multiplexly using the fundamental mode and the first-order mode of the PCNC, with the optimal RI and temperature sensitivities of 413 nm/RIU and 62.9 pm/K, and the corresponding detection limits of 7.2×10^{-6} RIU and 0.117 K, respectively. Large-dynamic-range sensing supported by the broad FSR is also analyzed. Therefore, due to the broad FSR, high Q, and ultracompact size, the proposed MM-PCNCs are promising platforms for realizing applications such as large-dynamic-range detection, high integration large scale on-chip sensing, and multifunctional detection in the future.

Index Terms: Photonic crystals, sensors, Photonic bandgap structures, Theory and design.

1. Introduction

Photonic crystal (PC) based optical sensing technologies especially of high integration on-chip sensing [1]–[11] and multifunctional detection [12]–[14] are attracting extensive attentions in these years. While most of the reported works focused on integration of multiple sensor units based on single-mode regime, with which one sensor unit only performs one function on one mode. In another aspect, multimode regime that considers taking full advantages of multiple

modes of the multimode cavity and enables more effective integration is still less reported in PC sensing applications. In the multimode regime, each resonant mode will be exploited as an independent sensing channel. In contrast, fibre based sensors have been targeting multimode regime for multi-parameter sensing for several years [15]–[20]. However challenges still exist for practical applications of those fibre based schemes, such as the unsatisfactory sensing accuracy, limited detection range, and inconvenient for further on-chip integration, each mainly because of the weak light localization, limited FSR, and microns level size of the fibre resonance device, respectively. Correspondingly, multimode PC resonance devices simultaneously with high Q, broad FSR, and ultra-compact size are exactly necessary for further improvements.

Here we propose a multimode regime based on-chip dual-parameter sensor platform using an ultra-compact multimode PCNC simultaneously with broad FSR and high Q. PCNC is selected as the platform because of its outstanding performances such as strong light controlling, flexible design, simple structure, ultra-compact size, easy fabrication, and compatibility with the photonic devices in strip waveguides [21]–[26]. In the multimode regime, multiple resonant modes are simultaneously used for multi-parameter sensing. While one challenge is that for most reported PCNCs based sensors, the integration and detection range are greatly limited by the modest FSR (usually around 5 nm-40 nm) of the resonant modes if not using any additional filters [8]–[11], [27]. As known, additional filters may add additional negative effects to the sensing system, such as inevitably leading to transmission reduction of the sensing signal, bringing additional complexity to the sensing system, increasing the difficulty for practical fabrication, and so on. Although works such as some 2D-PC or ring-based structures can sometimes obtain excellent FSR performance [28]–[32], but at the same time they put themselves in absolute inferiority with the huge size compared to 1D-PCNC based schemes.

In order to achieve PCNCs with broad FSR, the CLC is proposed by following some pre-band analysis. According to subtle design of the bands, CLC-PCNCs with distinct structural sensitivity of the dielectric mode band edges are obtained, enabling the excitation of multiple resonant modes with broad FSR possible. Furthermore, we report an interesting phenomenon that by tuning the band edges to approach to the contour line of the mirror strength (function of the band edges [23], [24], [33], [34]), the mirror strength eventually become stabilized in spite of the variation of specific structure parameter. The stabilized mirror strength will be verified of at least two benefits for the design: to further improve the FSR and the Q performances at an ultra-compact size.

Basing on the work above, MM-PCNCs simultaneous with broad FSR and high Q are successfully designed. With the maximum FSR exceeding 100 nm, we can realize applications like high integration multiplexing or large dynamic detection not only getting rid of the negative effects from additional filters, but also acquiring ultra-compact and simple design at the same time. Finally, basing on the multimode regime, simultaneous detection of the refractive index of air and the ambient temperature is conducted by multiplexly using the first two order modes of the proposed MM-PCNC. Simulation results show that sensitivities of 413.6 nm/RIU and 62.9 pm/K, with corresponding low detection limits of 7.2×10^{-6} RIU and 0.117 K, are obtained for the RI and temperature sensing, respectively. In addition, ultra-compact size of only about 220 nm $\times$ 550 nm $\times$ 10 um (height $\times$ width $\times$ length) is realized for the proposed PCNC, which is several times smaller compared to the 2D-PC, or ring based schemes [28]–[32]. Considering the broad FSR and stable performance in a wide spectral range, the proposed PCNC provides a promising platform for realizing applications such as large-dynamic-range detection, high integration on-chip sensing and multifunctional detection in the future.

The paper is organized as follows. In Section 2, we present the theoretical analysis and design of the broad FSR and high Q MM-PCNCs. Section 3 describes the sensing strategy and sensing performance in terms of sensitivity, detection range and limit of detection. The paper is summarized in Section 4.

abor holograms were numerically reconstructed over a range of image planes by sweeping the propagation distance.

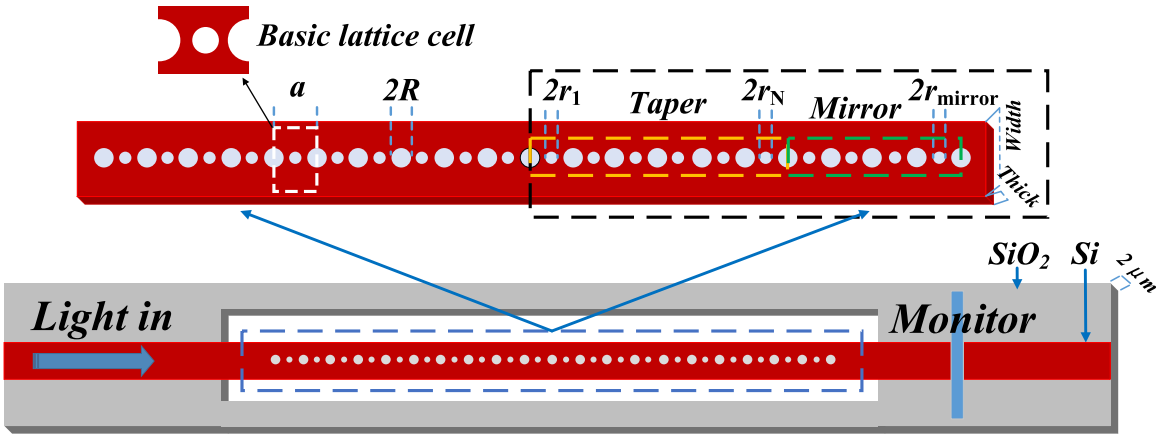

Fig. 1. Schematic of the whole sensor consisting of an air suspended PCNC supported by silica substrate at the in/out ends, with the proposed MM-PCNC shown in the blue dashed rectangle. The basic lattice cell (defined as CLC) is shown in the white dashed rectangle, and the taper section and additional mirror section are shown in the yellow and green dashed areas, respectively.

2. Design of MM-PCNC With Broad FSR and High Q

2.1 Basic Device Configuration

Fig. 1 shows the scheme and basic configuration of the proposed dual-parameter sensor based on a multi-mode PCNC. As seen, the sensor consists of an air suspended PCNC supported by silica substrate at the in/out ends of the propagation waveguide. Specifically, strip Si waveguide with a thickness (T) of 220 nm is considered in the work. The RI of the silicon waveguide and air holes at room temperature are $n_{si} = 3.46$ and $n_{air} = 1$, respectively. The proposed PCNC is formed by arranging the CLCs (shown in the white dashed rectangle in Fig. 1) with a constant 1D periodic of $a = 480$ nm in the guiding waveguide. The CLC consists of a smaller air hole ("S-hole") stuck in the middle of the two bigger ones ("L-hole"), whose radii are modulated as $r = r(i)$ and constant $R = 120$ nm, respectively. The width (W) of the guiding waveguide and nanobeam are set the same as $W = 550$ nm, which will benefit the mode match between the waveguide and the cavity. Specifically, the yellow dashed rectangle area and the green dashed rectangle area represent the taper section and the added mirror section, respectively. Additionally, the whole structure is symmetrical to the section in the black dashed rectangle area. The two symmetric halves of the left and right sides are set back to back without any extra distance in the middle so as to obtain the optimal Q performance [23], [24]. It is worth mentioning that owing to the specific structure of the CLC, more energy of the resonant modes will distribute in the low dielectric areas, which results in strong interaction between the light and matter, thus eventually contributing to the enhancement of RI sensitivities.

2.2 Theoretical Design and Results

Fig. 2(a) shows the band diagrams of the TE-polarized Bloch modes in the perfect CLC-PCNCs with different S-hole radius at a = 480 nm, $R = 120$ nm, $W = 550$ nm, and $T = 220$ nm. The calculations are conducted by using 3D-FDTD method with commercially available software from Lumerical Solutions [37]. The red, green, yellow and black curves are the band diagrams for the S-hole radius of $r = 90$ nm, 75 nm, 55 nm and 0 nm, respectively. The straight black line represents the light line in the air cladding. Specifically, the band edges located at wave vector of π/a that represent modes with the strongest energy of each bands are taken for further analysis [23] in Fig. 2(b)–(d). Fig. 2(b) shows the dielectric mode band edges with a sensitive response to the changes of the S-hole radius. Fig. 2(c) shows the contour map of mirror strength as functions of the band edges (f_2, f_1), where f_2 and f_1 represent the air mode and dielectric mode band edge, respectively. Fig. 2(d) shows the calculations of mirror strength versus the S-hole radius r. Here, the dielectric band

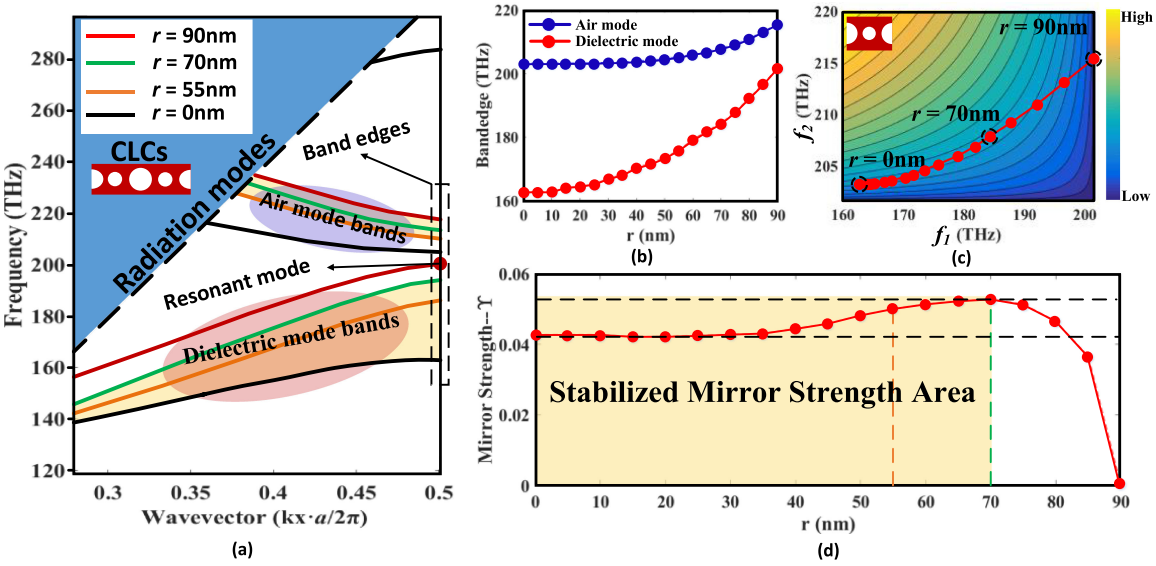

Fig. 2. (a) Band diagrams of perfect CLC-PCNCs with different S-hole radius. The lattice period a = 480 nm, strip Si waveguide width W = 550 nm, waveguide thickness T = 220 nm, constant L-hole radius R = 120 nm, and the S-hole radius r varies from 0 nm to 90 nm. The light blue and red elliptical area show the air mode and dielectric mode bands, respectively, with the band edges shown amplified in (b). (c) The band edges (f_2, f_1) stretch approaching to the contour line of mirror strength as functions of (f_2, f_1). The red dotted line, black solid lines, and the colour bar represent the band edges (f_2, f_1), mirror strength contour lines, and the magnitude of mirror strength, respectively. (d) The calculated mirror strength of PCNCs with different S-hole radius, with the target resonant frequency f_{res} = 201.6 THz at r = 90 nm.

edge for target resonance (with r = 90 nm) is located at 201.6 THz which deviates the desired resonance frequency 193.5 THz as a result of frequency perturbation [19]. It is noted that the CLC is proposed according to a method of trial and error, considering the principle that broader FSR originates from larger frequency intervals between the target resonant mode and its adjacent modes. As shown in Fig. 2(b), the dielectric mode band edge of the CLC-PCNC shows a distinct structural sensitivity which is conducive to generate broad frequency intervals with small amplitude structure modulations. As comparisons, most reported PCNCs with moderate FSR performance exhibited close-knit band edges (air mode or dielectric mode) in the band diagram [11], [35]–[38].

Generally, in order to obtain high-Q PCNCs, two aspects of optimizations are mainly focused on: one is to reduce the scattering loss into the free space, and the other is to reduce the propagation loss to the feeding waveguide [23], [24].

For reducing the scattering loss associated with abrupt changes in the modal distribution at the interfaces between the periodic segments and the propagation waveguide, we follow the deterministic design method proposed in [24], by creating a Gaussian-like attenuation profile, so as to minimize the spatial Fourier harmonics of the cavity mode inside the lightcone. The preferred Gaussian attenuation can be obtained from a Bragg mirror by making the mirror strength (denoted by the imaginary of the wavevector and indicating the EM field decay factor [23], [24], [33], [34]) a linearly increasing function of the position within the taper section. A segment with the target frequency is firstly determined as the central segment of the cavity, and then the mirror strength of each segment is calculated to find the segment with the maximum mirror strength as the end of the taper section. Definitely, the mirror strength is calculated by Eq. (1) [23], [24]:

$$\gamma = \sqrt{(f_2 - f_1)^2/(f_2 + f_1)^2 - (f_{res} - f_0)^2/f_0^2}. \quad (1)$$

Therein, f_2, f_1, f_0 are the air mode band edge, dielectric mode band edge and mid-gap frequency of each segment, respectively, and f_{res} is the target resonant frequency of the cavity. Firstly, r = 90 nm

is selected as the radius of S-hole in the central segment for localizing the resonant wavelength of the fundamental mode near 1550 nm, and the segment with the maximum mirror strength will be generally set as the end of the taper section. While different from most previous reported classical designs [11], [23], [24], [33]–[37], the mirror strength calculated in this work in Fig. 2(d) shows an interesting stability property in spite of quickly falling to zero after reaching the maximum value, which can be explained by the opposite monotone characteristic of γ versus f_1 *and* f_2 shown by Eq. (2)-(3):

$$\frac{d\gamma}{df_1} = \frac{\sqrt{f_2 - f_{res}}(f_1 - f_2 - 2f_{res})}{\sqrt{f_{res} - f_1}(f_1 + f_2)^2} \leq 0, \quad f_1 \leq f_{res} \leq f_2 \tag{2}$$

$$\frac{d\gamma}{df_2} = \frac{\sqrt{f_{res} - f_1}(f_1 - f_2 + 2f_{res})}{\sqrt{f_2 - f_{res}}(f_1 + f_2)^2} \geq 0, \quad f_1 \leq f_{res} \leq f_2 \leq 2f_{res} \tag{3}$$

where f_{res} is about 201 THz and f_2 is less than 300 THz, with the condition $f_2 \leq 2f_{res}$ meet easily. In a word, it is the mutual equilibrium of the opposite stretch trends of the dielectric band edges f_1 and the air band edges f_2 that makes the stability of the mirror strength possible.

To demonstrate it visually, Fig. 2(c) shows the contour map of γ versus (f_2, f_1) with the given target resonant frequency f_{res} and the condition of $f_1 \leq f_{res} \leq f_2$. The colour bar exhibits the mirror strength intensity, with the dark blue representing $\gamma = 0$. It's clear that as long as the band edges (f_2, f_1) approach to any one of the contour lines, the relevant mirror strength will remain. But it is not easy to find such a structure to achieve it. The proposed CLCs shown above and used in later design (for dielectric mode PCNC) are results of thousands of bands calculations, which should simultaneously satisfy at least the following three conditions: 1) $|d\gamma/df_1| \gg |d\gamma/df_2|$; 2) $f_2^{r_{\min}} > f_{res}$; 3) $[a - 2 \times (R + r_{\max})] > 10$ nm, with the first two conditions driving the band edges (f_2, f_1) approaching to the contour line, thus achieving the mirror strength stability, and the third condition ensuring enough gaps between the S-hole and L-hole in the lattice period, so as to control the difficulty for future practical fabrication. As seen, with the S-hole radius r decreasing from 90 nm to 0 nm, the band edge (f_2, f_1) first rises up from the zero line to higher lines, and arrives to the highest at $r =$ 70 nm, then goes down to the lower and finally gradually approaches to a line slightly lower than the highest but still above the zero. This matches well with the specific mirror strength varying type shown in Fig. 2(d) and visually explains why the stability of the mirror strength can be achieved. We will show that the special stability property will benefit much to further improving both of the FSR and Q performances, as well as minimizing the device size in the follow-up design.

Followly, the *r(i)* is quadratically modulated by Eq. (4) so as to approximately achieve linearly increased mirror strength with the segments away from the central segment in the taper section [23], [24]:

$$r(i) = r_1 - (r_1 - r_N) \times ((i - 1)/(N - 1))^2, \quad (1 \leq i \leq N) \tag{4}$$

where i and N represent the i-th segment and the total number of segments in the taper section, respectively, and r_1, r_N represent the radius of the S-hole of the first segment and the end segment in the taper section, respectively. More precisely, $r_1 = 90$ nm is set as the radius of S-hole in the central segment for localizing the resonant wavelength of the fundamental mode near 1550 nm. And due to some pre-conducted simulations, $N = 6$ is enough for the taper section, for the electric field distribution of the first two resonant modes will not exceed 6 segments in the direction along the waveguide at both sides. Note that N is better to be smaller in practice considering the miniaturization and simplification for the practical design and fabrication. Particularly, $r_N = 55$ nm is decided by the optimization to get an approximately linear increasing mirror strength from 0 (with $r_1 = 90$ nm) to the maximum (with r_5 about 70 nm) for the first several segments away from the central segment in the taper section, as shown by the red dotted dash line in the taper section in Fig. 3. Due to the mirror strength similarity, the sixth segment with $r = 55$ nm actually acts as an additional mirror. That r_N is set to be 55 nm rather than 70 nm directly is mainly for two considerations: the first is to widen the tapered range of the S-hole radius for easier fabrication, and the second is to further enlarge the frequency separation between the resonant mode and its adjacent modes, which will benefit

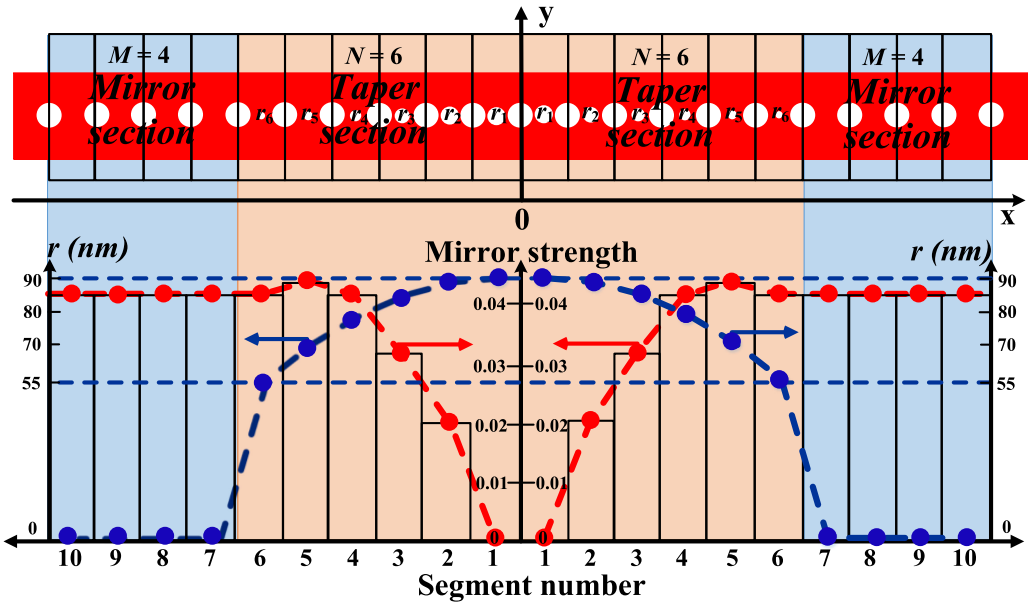

Fig. 3. Top: The schematic of the proposed PCNC, with $a = 480$ nm, $R = 120$ nm, $r_1 = 90$ nm, $r_N = 55$ nm, $r_{mirror} = 0$ nm, $N = 6$, $M = 4$, $W = 550$ nm, and $T = 220$ nm. Bottom: Mirror strength (red dotted line) and radius of the S-hole (blue dotted line) versus each segment of the PCNC in both of taper section and mirror section, respectively. The two blue dashed lines represent radius of the S-hole at 55 nm and 90 nm, respectively.

exciting modes with broader FSR. Therefore, broad-FSR dielectric-mode resonant modes can be excited by following the above settings, by gradually shifting the bandgap of each segment to lower frequency away from the center to the sides, leaving the dielectric mode bandedges of the central segments in the bandgaps of the side segments, thus eventually realizing the mode localization.

Then, in order to further reduce the propagation loss, additional segments with mirror strength same to the ending segment of the taper section will be generally added as mirrors to both sides of the taper section. While due to the special stability of the mirror strength achieved above, the S-holes radius of segments in the mirror section can be directly set constant as $r_{mirror} = 0$ nm rather than 55 nm. That is to say, no any S-holes are needed anymore. As shown in the mirror section in Fig. 3, the mirror strengths are maintained in spite of the r_{mirror} straightly going to zero. Figs. 4(a) and 4(b) show the quality factor and transmission property versus mirrors number M, with $R = 120$ nm, $r_1 = 90$ nm, $r_N = 55$ nm, $r_{mirror} = 0$ nm, $N = 6$, $W = 550$ nm, and $T = 220$ nm. As seen in the figure, with M increasing from 0 to 5, the Q value quickly increasing from the magnitude of 10^2 to 10^5, while the normalized transmission correspondingly decreases from nearly 1 to 0 at the same time. Therefore, $M = 4$ is taken for a balance between the Q value and the transmission, which exceed 2×10^4 and 0.2 for both of the fundamental mode and the first order mode, respectively. Note that the transmission at the cavity resonance can be written as $T = Q^2/Q_{wg}^2 = (Q_{rad}/(Q_{wg} + Q_{rad}))^2$, where $Q = Q_{rad}Q_{wg}/(Q_{wg} + Q_{rad})$, and Q_{rad}, Q_{wg} characterize the radiation loss into the free space and the propagation loss to the feeding waveguide, respectively [23]. With the number of mirror segments increasing, the Q is mainly limited by Q_{wg}, thus the transmission can be further approximated to be inversely related to Q_{wg}^2, which explains the Q improvement and the transmission reduction in Fig. 4(b).

Additionally, as verification, Figs. 5(a) and (b) show the FSR and Q performances as functions of r_{mirror} in the range from 55 nm to 0 nm, respectively. As seen in the figure, with the r_{mirror} decreasing, the Q value experiences relatively large increase from less than 2×10^4 to more than 5×10^4 for the fundamental mode, and from less than 1×10^4 to more than 2×10^4 for the first order mode, respectively. The FSR also shows slight increase with r_{mirror} decreasing, which exceeds 90 nm and

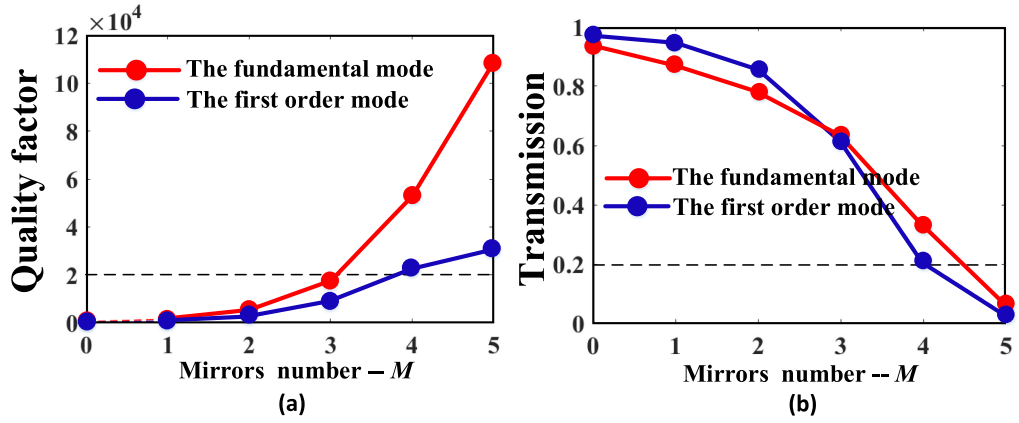

Fig. 4. (a) Quality factor and (b) Transmission of the MM-PCNC versus different amount of segments in the mirror section, with $a = 480$ nm, $R = 120$ nm, $r_1 = 90$ nm, $r_N = 90$ nm, $r_{mirror} = 0$ nm, $N = 6$, $W = 550$ nm, and $T = 220$ nm. The red and blue dotted lines represent results of the fundamental mode and the first order mode, respectively. The dark dashed lines indicate $Q > 2 \times 10^4$ and Transmission >0.2 in (a) and (b), respectively.

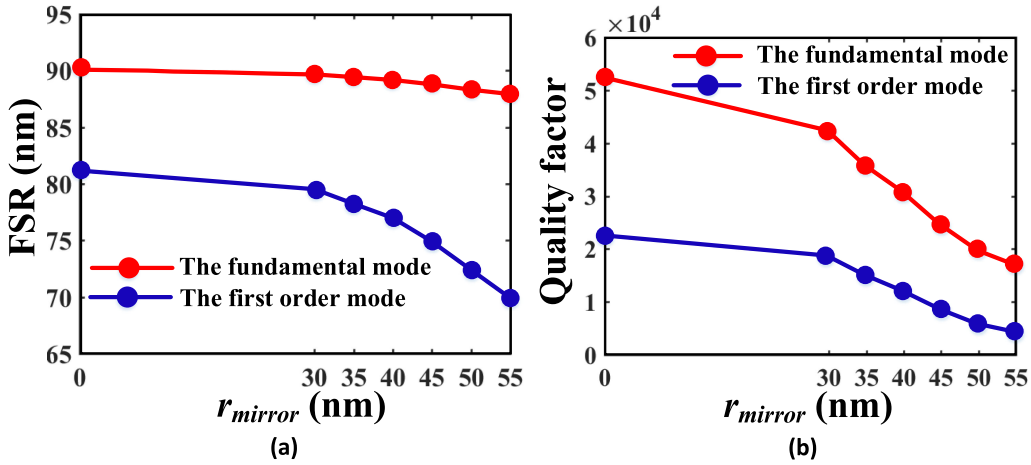

Fig. 5. (a) FSR and (b) Q performances of the MM-PCNC versus r_{mirror} of segments in the mirror section, with $a = 480$ nm, $R = 120$ nm, $r_1 = 90$ nm, $r_N = 90$ nm, $N = 6$, $M = 4$, $W = 550$ nm, and $T = 220$ nm. The red and blue dotted lines represent results of the fundamental mode and the first order mode, respectively.

80 nm at $r_{mirror} = 0$ nm for both of the two resonant modes, respectively. Therefore, $r_{mirror} = 0$ nm is verified to be the optimal setting for obtaining PCNCs with the best performances of FSR and Q, as well as the simplest structure. Thus, the special mirror strength stability achieved in this work is demonstrated to be beneficial at least two aspects for the design: simpler structure with better performances.

Therefore, according to the elaborate design shown above, ultra-compact (only 10 segments at each side) MM-PCNCs simultaneously with broad FSR (90.13 nm and 81.11 nm) and high Q (52549.5 and 22410.4) for the fundamental mode and the first order mode have been finally obtained (as shown in Fig. 6(b)). Fig. 6(a) shows the optimal structure of the design, with $R = 120$ nm, $r_1 = 90$ nm, $r_N = 55$ nm, $r_{mirror} = 0$ nm, $N = 6$, $M = 4$, $W = 550$ nm, and $T = 220$ nm. Fig. 6(c) shows the corresponding field distribution profiles (|Ey|) in x-y plane at $z = 0$ for the first two order resonant modes. As seen, the fields of the modes are mainly distributed in the air holes. In order to quantitatively demonstrate the interaction between the light and matter, the light overlap integral

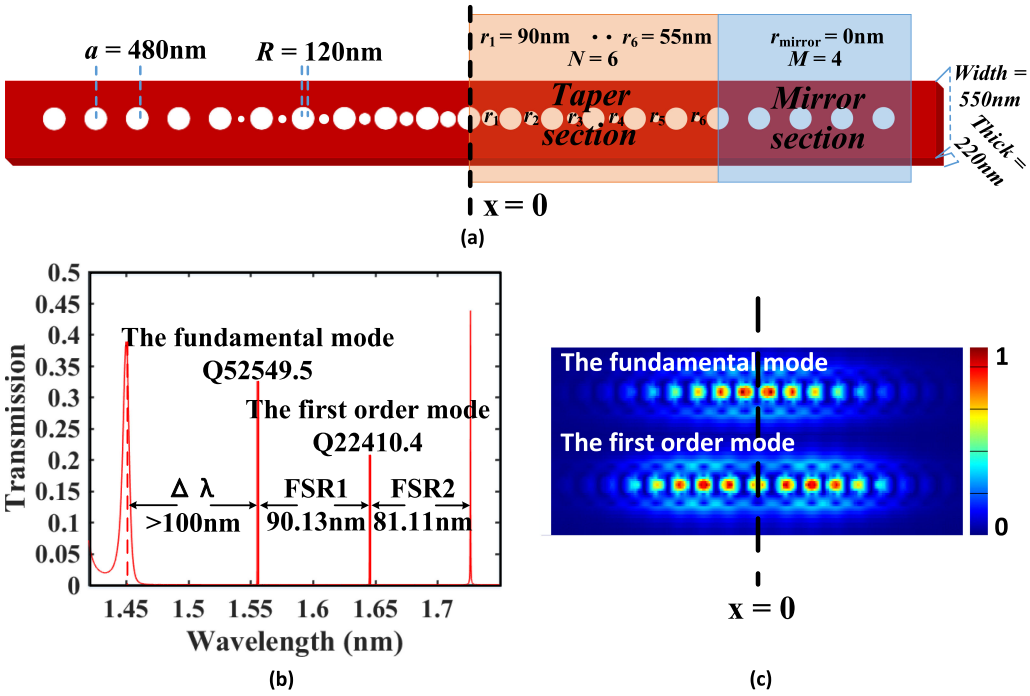

Fig. 6. (a) The schematic of the final MM-PCNC, with $a = 480$ nm, $R = 120$ nm, $r_1 = 90$ nm, $r_{mirror} = 0$ nm, $N = 6$, $M = 4$, $W = 550$ nm, and $T = 220$ nm. (b) 3D-FDTD composed transmission of the optimized MM-PCNC. $\Delta\lambda$ is the separation between the fundamental mode and the band edge modes. (c) Electric field distribution profiles ($|E_y|$) in x-y plane at z = 0 for the fundamental mode and the first order mode, respectively. Black dashed line indicates the center of cavity along the propagation direction. Colour bar represents the intensity of fields, in which dark blue and dark red represent the weakest and the strongest intensity, respectively.

f as the ratio of electric field energy in analyte region (air in our case) to the total energy for a given mode is defined and calculated by Eq. (5) [39], [40]:

$$f = \int_{V_{analyte}} \xi |E|^2 dr^3 / \int_{V_{analyte+dielectric}} \xi |E|^2 dr^3, \tag{5}$$

where ξ represents the dielectric constant of the material. Results show that the overlap integrals f are as high as 27.62% and 28.32% for the fundamental mode and the first order mode, respectively. As known, higher overlap integral represents more effective interaction between the light and matter, thus contributing to higher RI sensitivity. It will be shown later in Fig. 8(a) that the RI sensitivity of the first order mode is higher than the fundamental mode, which can be explained by the slightly higher overlap integral of the former.

It should be mentioned that for the convenience of discussion, only the first two order modes are analyzed above, and more resonant modes can be considered in the same way if needed. Also, in order to further verify the rationality of the selection of r_N as 55 nm in spite of 70 nm in the former setting, we did additional simulations to exhibit the performances of FSR and Q versus r_N, as shown in Fig. 7. Note that r_N less than 30 nm is not considered in the analysis considering the difficulty for practical fabrication. Fig. 7(a) shows that with r_N gradually decreasing from 70 nm to 30 nm, the FSRs of the fundamental mode and the first order mode correspondingly increase from 76.17 nm to 107.09 nm, and from 72.41 nm to 92.41 nm, respectively, meanwhile, the Q values in Fig. 7(b) maintain high above 2×10^4 and 1×10^4, respectively. The FSR is broadened because of the enlarged separations between the adjacent dielectric mode band edges when the taper range is increased with an unchanged N. And the Q is impaired because of the actual number reduction of the segments in the mirror strength taper section. Specifically, with r_N in the range from 30 nm

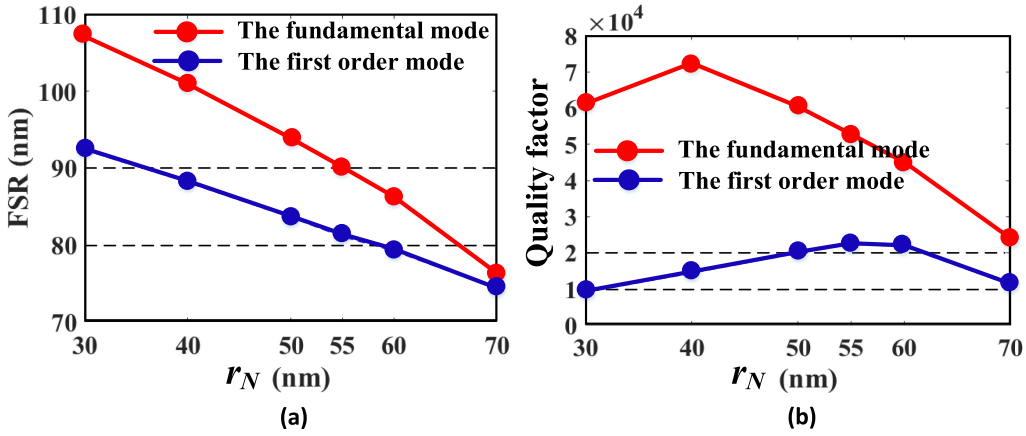

Fig. 7. (a) FSR and (b) Quality factor value of the MM-PCNC versus S-hole radius r_N of the ending segment in the taper section, with $R = 120$ nm, $r_1 = 90$ nm, $r_{mirror} = 0$ nm, $N = 6$, $M = 4$, $W = 550$ nm, and $T = 220$ nm. Black dashed lines in (a) indicate FSR >90 nm and FSR >80 nm, respectively. Black dashed lines in (b) indicate Q > 2×10^4 and Q > 1×10^4, respectively. Red and blue dashed line connected points represent results of the fundamental mode and the first order mode, respectively.

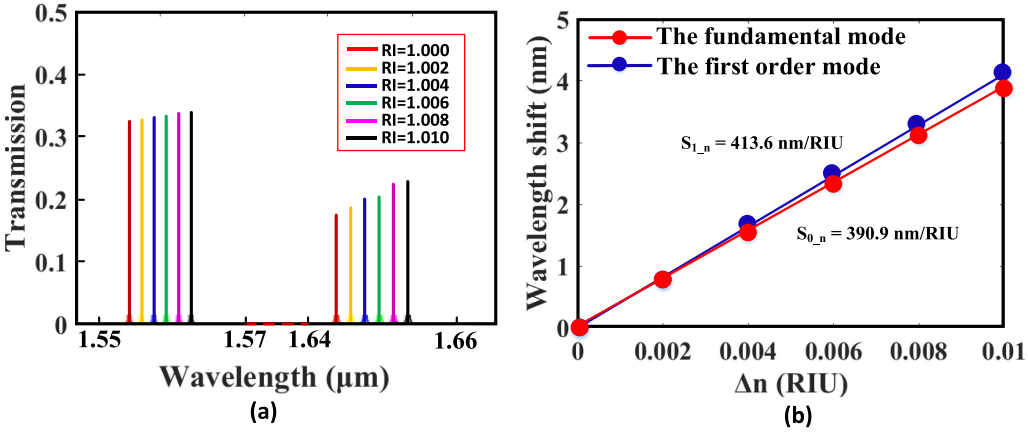

Fig. 8. (a) 3D-FDTD composed transmission spectra observed when the sensor is subjected to RI variations of air, at constant K = 300. (b) Fitted results of wavelength shifts versus RI variations for the fundamental mode and the first order mode, respectively.

to about 55 nm, PCNCs simultaneous with FSR above 90 nm and 80 nm and Q above 5×10^4 and 1×10^4 are realized for the fundamental mode and the first order mode, respectively. And the fundamental mode achieves its broadest FSR (107.09 nm) at $r_N = 30$ nm and the first order mode reaches its optimal Q performance at about $r_N = 55$ nm, respectively. Considering the broad FSR achieved, the proposed PCNCs are very suitable for realizing applications such as large dynamic range sensing and high integration multiplexing with more effective design and more compact size, with no additional filters needed after all.

Another important notation is that all the performances achieved above are on the premise of keeping an ultra-compact size for the device ($N = 6$, $M = 4$). Higher Q is predicable with further optimizations such as just adding segments on both sides of the cavity (further 3D-FDTD simulations show that Q $\sim 10^7$ can be obtained just with $N = 16$, $M = 6$, and even higher with more segments, not shown here). While it may be not necessary because the Q at the magnitude of 10^4 (such as 5×10^4 and 2×10^4 for the first two modes in this work) are already high enough for most sensing applications, and even not recommended because a longer resonance cavity is not conducive to

the signal light transmission and will weaken the mechanical stability. Overall, we provide a new perspective to optimize the PCNCs, with better performances (Q and FSR) and smaller size, which can serve as a guide for future designs such as PCNCs in liquid environment. And experimental work will be done in future, considering the experimental conditions are not yet satisfied for us at the moment.

3. Analysis for Dual-Parameter Sensing

Basing on the designed MM-PCNCs shown in Fig. 6, we further discuss the application in multi-parameter sensing in this section. Generally, in order to detect more than one parameter at one time, the most popular technology is multiplexing, or called multi-channel or multi-cavity multiplexing, which has been widely used in previous works [1]–[11]. And multifunctional schemes like on-chip dual parameter sensor based on two reference channels or cavities are also reported [12]–[14]. For further minimization and simplification of the design, some single cavity (channel) based multi-parameter sensor such as sensors by simultaneously taking advantages of the sensing properties of the imaginary and real parts of RI of the liquid [41] or simultaneously stimulating TE and TM modes in a multi-mode cavity [42] have also been reported in recent years. However, with the moderate sensitivity (less than 200 nm/RIU) in [41] or ultra-limited FSR (only around 5 nm) in [42], they are still facing difficulties in further practical application. Here, we propose a dual-parameter sensor by multiplexly using the first two order modes of the designed MM-PCNC. Specifically, simultaneous detection of variations of the RI of air and the ambient temperature are theoretically analysed. Compared to most previous works, our work shows advantages in ultra-compact size, broad spectra range for sensing, low detection limit, and relatively high RI sensitivity.

For the dual-parameter sensing, the sensing performance can be described by defining a sensor matrix as follows:

$$\mathrm{S_{mat}} = \begin{bmatrix} S_{0\_n} & S_{0\_T} \\ S_{1\_n} & S_{1\_T} \end{bmatrix}, \tag{6}$$

where S_{0_n} and S_{0_T} are the sensitivities of RI and temperature for the fundamental mode, respectively, and S_{1_n} and S_{1_T} are the sensitivity of RI and temperature for the first order mode, respectively. Then the sensing process can be described as:

$$\begin{bmatrix} \Delta\lambda_0 \\ \Delta\lambda_1 \end{bmatrix} = \mathrm{S_{mat}} \begin{bmatrix} \Delta n \\ \Delta T \end{bmatrix}, \tag{7}$$

where $\Delta\lambda_0$ and $\Delta\lambda_1$ represent the wavelength shifts of the fundamental mode and the first order mode as responses to the variations of RI (Δn) and temperature (ΔT), respectively. Thus, if $|S_{\mathrm{mat}}| \neq 0$, the variations of RI and temperature can be calculated by:

$$\begin{bmatrix} \Delta n \\ \Delta T \end{bmatrix} = \mathrm{S}_{mat}^{-1} \begin{bmatrix} \Delta\lambda_0 \\ \Delta\lambda_1 \end{bmatrix}. \tag{8}$$

Formula (8) shows that the dual-parameter sensing in nature is still realized by detecting the wavelength responses (shifts) to the environment changes, so as long as there is no spectrum overlap between the two exploited modes in the sensing, the detection can be in theory realized.

Firstly, the wavelength responses of different RI with constant temperature at 300 K are analyzed. Fig. 8(a) shows the transmission of the resonant wavelength with RI of air varying from 1.000 to 1.010 with a step of 0.002. As seen in the figure, both of the two resonant peaks show blue shift as the RI increases. Fig. 8(b) shows the liner fitting of resonant wavelength shift versus RI variations of the fundamental and the first order mode, respectively, from which the sensitivities $S_{0\_n} = 390.9$ nm/RIU and $S_{1\_n} = 413.6$ nm/RIU are calculated for the two modes, respectively. Also, the detection limits (DL) are theoretically calculated by the formula $\mathrm{DL} = \lambda_{\mathrm{res}}/ (10 \times \mathrm{Q} \times \mathrm{S})$ [43], of which the results are 7.6×10^{-6} RIU and 7.2×10^{-6} RIU for the fundamental mode and the first order mode, respectively.

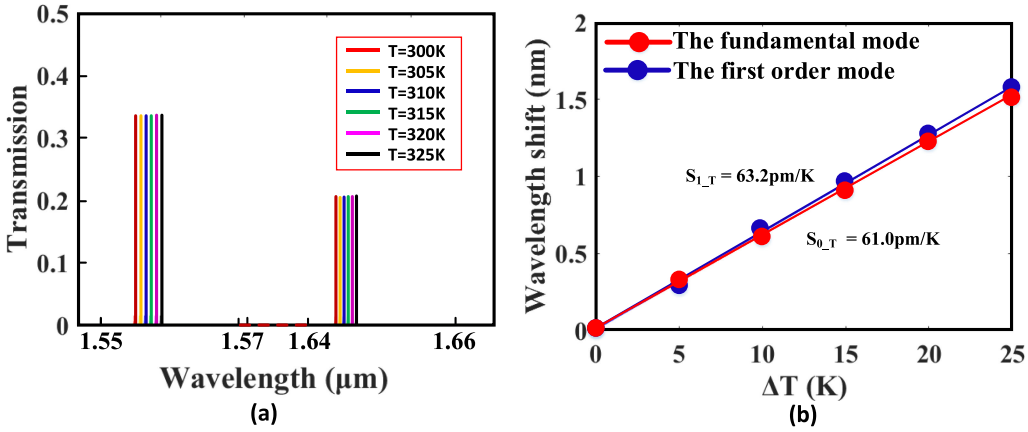

Fig. 9. (a) 3D-FDTD composed transmission spectra observed when the sensor is subjected to temperature, with RI = 1.000RIU. (b) Fitted results of wavelength shifts versus temperature variations for the fundamental mode and the first order mode, respectively.

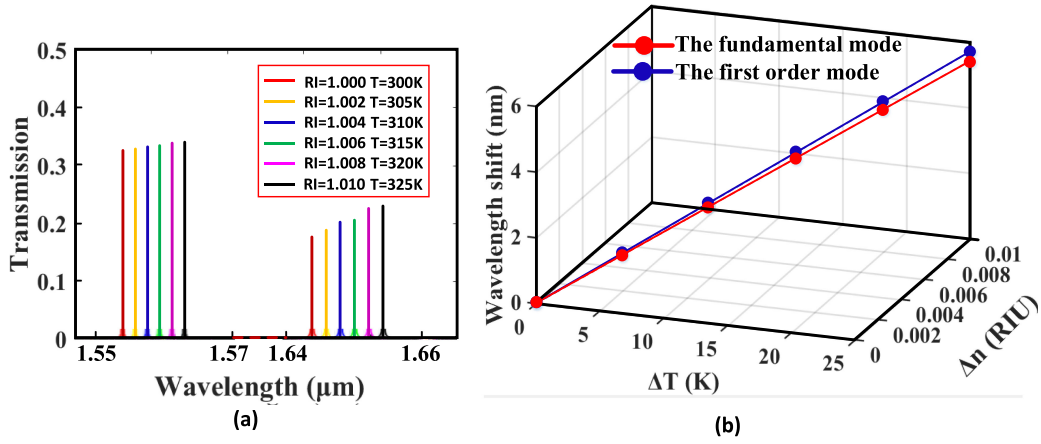

Fig. 10. (a) Transmission spectra observed when the sensor is simultaneously subjected to both of the RI and temperature variations. (b) Wavelength shifts versus refractive index and temperature variations for the fundamental mode and the first order mode, respectively.

Then, with a constant RI = 1.000, the temperature responses of the sensor are demonstrated. It should be noted that considering the thermos-optic coefficient of air ($\sim 10^{-7}$ RIU/K) [44]–[47] and the thermos-expansion of Si ($\sim 10^{-6}$ RIU/K) [48] are low enough to be ignored compared to the thermos-optic coefficient of Si ($\sim 1.8 \times 10^{-4}$ RIU/K) [49], so the temperature response is calculated by only exerting thermal index perturbation to the Si waveguide in simulation. Correspondingly, Fig. 9(a) shows the transmission spectra of the resonant wavelength with the ambient temperature varying from 300 K to 325 K. Moreover, the fitted results of the wavelength shifts are shown in Fig. 9(b), from which sensitivities of $S_{0\_T} = 60.7$ pm/K and $S_{0\_T} = 62.9$ pm/K can be calculated for the fundamental mode and the first order mode, respectively. Correspondingly, the detection limits for the two modes are 0.121 K and 0.117 K, respectively.

Finally, for the dual-parameter sensing, simultaneous variations of the RI and temperature are conducted, with the overall wavelength reaction shown in Figs. 10(a) and (b). Here, for convenience of comparison, both the RI and temperature are set in a one-to-one correspondence in ranges same to the settings in the single parameter sensing. From Fig. 10(b), we can see that the wavelength responses to the simultaneous variations of the RI and the temperature are also well consistent with the linear relationship. Thus, with the sensitivities of RI (S_{0_n} and S_{1_n}) and temperature (S_{0_T} and

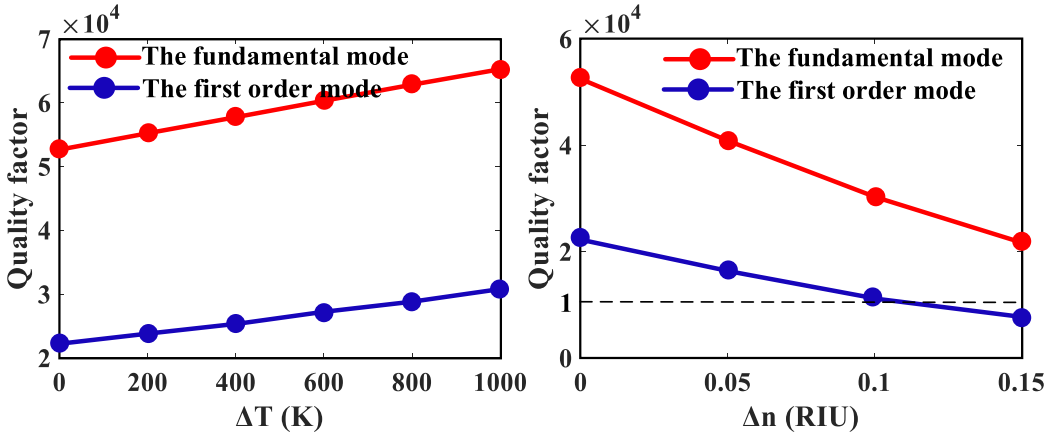

Fig. 11. Q of the proposed sensor versus (a) ΔT and (b) Δn, respectively. Blue and red dotted lines represent the fundamental mode and the first order mode, respectively. The black dashed line in (b) indicates the Q above 1×10^4.

S_{1_n}) pre-obtained in the single parameter sensing, once the wavelength shifts of the fundamental mode ($\Delta\lambda_0$) and the first order mode ($\Delta\lambda_1$) are measured, the variations of RI (Δn) and temperature (ΔT) can be mathematically estimated by solving the following matrix equation:

$$\begin{bmatrix} \Delta n \\ \Delta T \end{bmatrix} = \begin{bmatrix} 390.9\ \text{nm}/RIU & 60.7\ \text{pm}/K \\ 413.6\ \text{nm}/RIU & 62.9\ \text{pm}/K \end{bmatrix}^{-1} \begin{bmatrix} \Delta\lambda_0 \\ \Delta\lambda_1 \end{bmatrix} \tag{9}$$

Furthermore, the sensor is exhibited to be very suitable for large dynamic range sensing, not only because of its broad FSR, but also because of the maintained performances in wide variation ranges for both of the temperature and RI. As shown in Fig. 11(a), the Q of the PCNC is slightly enhanced by the increased temperature, with a predictable linear relationship in a range more than 1000 K. Considering the melting point of silicon (1600 K) and the total wavelength shift of about 60 nm (<FSR2<FSR1) for $\Delta T = 1000$ K, the sensor could in theory detect the variation of temperature in an ultra-large dynamic range more than 1000 K. Fig. 11(b) shows that the Q value of the proposed PCNC maintains high above 1×10^4 despite the RI increases from 1.000 RIU to 1.100 RIU, also with the calculated wavelength shift (~40 nm) not exceeding the FSRs of the modes, which means the sensor could in theory detect the variation of RI in an ultra large-dynamic-range no less than 0.100 RIU. This range almost coves the maximum RI of gaseous substances. Therefore, the proposed sensor shows promising prospects in large dynamic range sensing for both of the RI and temperature. Further experimental work will be done once the laboratory conditions permit.

Finally, there are still two points to note for the above analysis. Firstly, because the proposed structure is relatively sophisticated, the device will inevitably suffer from the practical fabrication, such as the Q performance will predictably degrade due to the fabrication error. Thus according to the definition of the defection limit in the manuscript ($DL = \lambda res/(10 \times Q \times S)$), the claimed detection limits of both of the RI and temperature will be weakened to some extent in the practical application. Secondly, in fact, in order to achieve the declared sensing performances (such as the detection limit), except for considering the influence of the manufacturing error of the device, what is more important is the anti-interference property of the sensor, that is, the ability to overcome or resist the various disturbances in the sensing process (such as interference from the non-measured variables in the environment, the possible interference between the modes, the system errors, reading errors, etc.). Because once fabricated, the optical performance of the device is basically determined. Thus in practical applications, whether the multi-parameter sensor can finally achieve effective or accurate detection is up to whether the sensor can resist the above-mentioned various disturbances in the sensing process. Therefore, to further improve the structure stability of

the optical performance of the device (such as the Q) and to further improve the above-mentioned anti-interference property of the sensor are two crucial points for the practical application of the proposed multimode dual-parameter sensor in the future.

4. Conclusions

In summary, we first provided a method for designing multimode PCNCs simultaneously with broad FSR and high Q, and then applied it for dual parameter sensing by using the multimode regime. The principles of enlarging the frequency separations among the specific mode (dielectric mode in this work) band edges, and tuning the band edges (f_2, f_1) to approach to the contour line of the mirror strength are key to achieve PCNC with broad FSR, high Q, as well as compact size. Due to the mirror strength stability, the Q values can be further improved for more than two times for both of the first two order modes compared to PCNCs with general mirrors, at the same time with a simplified structure. Besides, strong interactions between the modes and matter are obtained and quantitatively analysed by the calculated light overlap integrals (close to 30%) and the RI sensitivities (around 400/RIU), respectively. Compared to most previous multi-cavity, multi-channel, or fibre based multi-parameter sensing schemes, the proposed dual-parameter sensor shows advantages in ultra-compact size (220 nm $\times$ 550 nm $\times$ 10 um) for effective integration, high Q for accurate measurement (detection limits for the RI and temperature sensing are 7.2×10^{-6}RIU and 0.117 K, respectively), and broad FSR for large dynamic range sensing, respectively. Overall, the work provides a new perspective for the design of broad FSR and high Q photonic devices, and shows promising potentials for realizing applications such as large-dynamic-range sensing, high integration large-scale on-chip sensing and multifunctional detection in the future.

References

[1] S. Mandal and D. Erickson, "Nanoscale optofluidic sensor arrays," *Opt. Exp.*, vol. 16, pp. 1623–1631, 2008.
[2] D. Yang, H. Tian, and Y. Ji, "Nanoscale low crosstalk photonic crystal integrated sensor array," *IEEE Photon. J.*, vol. 6, no. 1, pp. 1–7, Feb. 2014.
[3] L. Huang, H. Tian, J. Zhou, and Y. Ji, "Design low crosstalk ring-slot array structure for label-free multiplexed sensing," *Sensors (Basel)*, vol. 14, no. 9, pp. 15658–15668, 2014.
[4] D. Yang, H. Tian, N. Wu, Y. Yang, and Y. Ji, "Nanoscale torsion-free photonic crystal pressure sensor with ultra-high sensitivity based on side-coupled piston-type microcavity," *Sens. Actuators A*, vol. 199, pp. 30–36, 2013.
[5] J. Zhou, L. Huang, Z. Fu, F. Sun, and H. Tian, "Higher Q factor and higher extinction ratio with lower detection limit photonic crystal–parallel-integrated sensor array for on-chip optical multiplexing sensing," *Appl. Opt.*, vol. 55, pp. 10078–10083, 2016.
[6] H. Yan *et al.*, "Silicon on-chip bandpass filters for the multiplexing of high sensitivity photonic crystal microcavity biosensors," *Appl. Phys. Lett.*, vol. 106, no. 12, 2015, Art. no. 121103.
[7] H. Yan *et al.*, "Specific detection of antibiotics by silicon on-chip photonic crystal biosensor arrays," *IEEE Sensors J.*, vol. 17, no. 18, pp. 5915–5919, Sep. 2017.
[8] D. Yang, C. Wang, and Y. Ji, "Silicon on-chip 1D photonic crystal nanobeam bandstop filters for the parallel multiplexing of ultra-compact integrated sensor array," *Opt. Exp.*, vol. 24, no. 15, pp. 16267–16279, 2016.
[9] P. B. Deotare, L. C. Kogos, I. Bulu, and M. Lončar, "Photonic crystal nanobeam cavities for tunable filter and router applications," *IEEE J. Sel. Topics Quantum Electron.*, vol. 19, no. 2, 2013, Art. no. 3600210.
[10] J. Zhou, L. Huang, Z. Fu, and H. Tian, "Multiplexed simultaneous high sensitivity sensors with high-order mode based on the integration of photonic crystal 1 $\times$ 3 beam splitter and three different single-slot PCNCs," *Sensors*, vol. 16, no. 7, 2016, Art. no. 1050.
[11] F. Sun, Z. Fu, C. Wang, Z. Ding, C. Wang, and H. Tian, "Ultra-compact air-mode photonic crystal nanobeam cavity integrated with bandstop filter for refractive index sensing," *Appl. Opt.*, vol. 56, no. 15, pp. 4363–4368, 2017.
[12] Y. Chen, H. Liu, Z. Zhang, A. Gupta, and M. Yu, "Planar photonic crystal based multifunctional sensors," *Appl. Opt.*, vol. 56, pp. 1775–1780, 2017.
[13] Y. N. Zhang, Y. Zhao, and H. F. Hu, "Miniature photonic crystal cavity sensor for simultaneous measurement of liquid concentration and temperature," *Sens. Actuator Biol. Chem.*, vol. 216, pp. 563–571, 2015.
[14] P. Liu and Y. Shi, "Simultaneous measurement of refractive index and temperature using cascaded side-coupled photonic crystal nanobeam cavities," *Opt. Exp.*, vol. 25, no. 23, 2017, Art. no. 28398.
[15] I. Jung, B. Park, J. Provine, R. Howe, and O. Solgaard, "Highly sensitive monolithic silicon photonic crystal fiber tip sensor for simultaneous measurement of refractive index and temperature," *J. Lightw. Technol.*, vol. 29, no. 9, pp. 1367–1374, May 2011.
[16] Y. Miao *et al.*, "Simultaneous measurement of temperature and magnetic field based on a long period grating concatenated with multimode fiber," *Appl. Phys. Lett.*, vol. 106, no. 13, 2015, Art. no. 132410.

[17] C. Lin *et al.*, "Liquid modified photonic crystal fiber for simultaneous temperature and strain measurement," *Photon. Res.*, vol. 5, no. 2, pp. 129–133, 2017.
[18] A. Lopez-Aldaba, J. Auguste, and R. Jamier, "Simultaneous strain and temperature multipoint sensor based on microstructured optical fiber," *J. Lightw. Technol.*, vol. 36, no. 4, pp. 910–916, Feb. 2018.
[19] J. Hu, T. Lang, and G. Shi, "Simultaneous measurement of refractive index and temperature based on all-dielectric metasurface," *Opt. Exp.*, vol. 25, no. 13, pp. 15241–15251, 2017.
[20] R. Xing, C. Dong, Z. Wang, W. Yue, Y. Yang, and S. Jian, "Simultaneous strain and temperature sensor based on polarization maintaining fiber and multimode fiber," *Opt. Laser Technol.*, vol. 102, pp. 17–21, 2018.
[21] P. B. Deotare, M. W. McCutcheon, I. W. Frank, M. Khan, and M. Lončar, "High quality factor photonic crystal nanobeam cavities," *Appl. Phys. Lett.*, vol. 94, no. 12, 2009, Art. no. 121106.
[22] I. Frank, P. Deotare, M. McCutcheon, and M. Lončar, "Programmable photonic crystal nanobeam cavities," *Opt. Exp.*, vol. 18, no. 8, pp. 8705–8712, 2010.
[23] Q. Quan, P. B. Deotae, and M. Loncar, "Photonic crystal nanobeam cavity strongly coupled to the feeding waveguide," *Appl. Phys. Lett.*, vol. 96, no. 20, 2010, Art. no. 203102.
[24] Q. Quan and M. Loncar, "Deterministic design of wavelength scale, ultra-high Q photonic crystal nanobeam cavities," *Opt. Exp.*, vol. 19, no. 19, pp. 18529–18542, 2011.
[25] P. Lin, T. Lu, and P. Lee, "Photonic crystal waveguide cavity with waist design for efficient trapping and detection of nanoparticles," *Opt. Exp.*, vol. 22, no. 6, pp. 6791–6800, 2014.
[26] S. Han and Y. Shi, "Systematic analysis of optical gradient force in photonic crystal nanobeam cavities," *Opt. Exp.*, vol. 24, no. 1, pp. 452–458, 2016.
[27] D. Yang, C. Wang, and Y. Ji, "Silicon on-chip one-dimensional photonic crystal nanobeam bandgap filter integrated with nanobeam cavity for accurate refractive index sensing," *IEEE Photon. J.*, vol. 8, no. 2, Apr. 2016, Art. no. 4500608.
[28] Z. Ding, J. Zhou, L. Huang, F. Sun, Z. Fu, and H. Tian, "Design of side-coupled cascaded photonic crystal sensors array with ultra-high figure of merit," *Opt. Commun.*, vol. 392, pp. 68–72, 2017.
[29] N. Eid, R. Boeck, H. Jayatilleka, L. Chrostowski, W. Shi, and N. Jaeger, "FSR-free silicon-on-insulator microring resonator based filter with bent contra-directional couplers," *Opt. Exp.*, vol. 24, no. 25, pp. 29009–29021, 2016.
[30] D. Urbonas *et al.*, "Ultra-wide free spectral range, enhanced sensitivity, and removed mode splitting SOI optical ring resonator with dispersive metal nanodisks," *Opt. Lett.*, vol. 40, no. 13, pp. 2977–2980, 2015.
[31] S. Xiao, M. Khan, H. Shen, and M. Qi, "A highly compact third-order silicon microring add-drop filter with a very large free spectral range, a flat passband and a low delay dispersion," *Opt. Exp.*, vol. 15, no. 22, pp. 14765–14771, 2007.
[32] Y. Hung, C. Wu, T. Chen, T. Yen, and Y. Liang, "Superior temperature-sensing performance in cladding-modulated si waveguide gratings," *J. Lightw. Technol.*, vol. 34, no. 18, pp. 4329–4335, Sep. 2016.
[33] L. Huang, J. Zhou, F. Sun, Z. Fu, and H. Tian, "Optimization of one dimensional photonic crystal elliptical-hole low-index mode nanobeam cavities for on-chip sensing," *J. Lightw. Technol.*, vol. 34, no. 15, pp. 3496–3502, Aug. 2016.
[34] A. Bazin, R. Raj, and F. Raineri, "Design of silica encapsulated high-Q photonic crystal nanobeam cavity," *J. Lightw. Technol.*, vol. 32, no. 5, pp. 952–958, Mar. 2014.
[35] B. Desiatov, I. Goykhman, and U. Levy, "Parabolic tapered photonic crystal cavity in silicon," *Appl. Phys. Lett.*, vol. 100, no. 4, 2012, Art. no. 041112.
[36] J. Zhou, H. Tian, L. Huang, Z. Fu, F. Sun, and Y. Ji, "Parabolic tapered coupled two photonic crystal nanobeam slot cavities for high-FOM biosensing," *IEEE Photon. Technol. Lett.*, vol. 29, no. 16, pp. 1281–1284, Aug. 2017.
[37] Lumerical Solutions, Inc., [Online]. Available: http://www.lumerical.com
[38] W. Zhang, S. Serna, X. Roux, L. Vivien, and E. Cassan, "Silicon nanobeam cavity for ultra-localized light-matter interaction," *Opt. Lett.*, vol. 42, no. 17, pp. 3323–3326, 2017.
[39] L. Huang *et al.*, "Improving the detection limit for on-chip photonic sensors based on subwavelength grating racetrack resonators," *Opt. Exp.*, vol. 25, no. 9, pp. 10527–10535, 2017.
[40] Y. Liu, S. Wang, D. Zhao, W. Zhou, and Y. Sun, "High quality factor photonic crystal filter at k$\sim$0 and its application for refractive index sensing," *Opt. Exp.*, vol. 25, no. 9, pp. 10536–10545, 2017.
[41] X. Zhang *et al.*, "On-chip integrated optofluidic complex refractive index sensing using silicon photonic crystal nanobeam cavities" *Opt. Lett.*, vol. 41, no. 6, pp. 1197–1200, 2016.
[42] P Liu and Y Shi, "Simultaneous measurement of refractive index and temperature using a dual polarization ring," *Appl. Opt.*, vol. 55, no. 13, pp. 3537–3541, 2016.
[43] I. White and X. Fan, "On the performance quantification of resonant refractive index sensors," *Opt. Exp.*, vol. 16, no. 2, pp. 1020–1028, 2008.
[44] D. Wang, B. Xu, and Y. Liu, "Optical fiber Fabry-Pérot interferometer based on an air-cavity for gas pressure sensing," *IEEE Photon. J.*, vol. 9, no. 2, Apr. 2017, Art. no. 7102309.
[45] Y. Yu, X. Chen, Q. Huang, C. Du, S. Ruan, and H. Wei, "Enhancing the pressure sensitivity of a Fabry-perot interferometer using a simplified hollow-core photonic crystal fiber with a microchannel," *Appl. Phys. B*, vol. 130, no. 3, pp. 461–467, 2015.
[46] J. Owens, "Optical refractive index of air: dependence on pressure, temperature and composition," *Appl. Opt.*, vol. 6, no. 1, pp. 51–59, 1967.
[47] P. Ciddor, "Refractive index of air: New equations for the visible and near infrared," *Appl. Opt.*, vol. 35, no. 9, pp. 1566–1573, 1996.
[48] H. Watanabe, N. Yamada, and M. Okaji, "Linear thermal expansion coefficient of silicon from 293 to 1000 K," *Int. J. Thermophysics*, vol. 25, no. 1, pp. 221–236, 2004.
[49] C. Y. Jiang, P. T. S. DeVore, C. K. Lonappan, and J. Adam, "SiCloud: An online education tool for silicon photonics," in *Proc. Conf. Edu. Training Opt. Photon.*, 2017, p. 41.